

Two categories of UV-upturn galaxies revealed by semi-analytic models

Zhen Jiang,^{1,2*} Cheng Li,^{1 †} Fenghui Zhang,^{3,4,5} and Shuang Zhou⁶

¹Department of Astronomy, Tsinghua University, Beijing 100084, China

²National Astronomical Observatories, Chinese Academy of Sciences, Beijing 100101, China

³Yunnan Observatories, Chinese Academy of Sciences, Kunming, 650216, China

⁴Key Laboratory for the Structure and Evolution of Celestial Objects, Chinese Academy of Sciences, Kunming, 650216, China

⁵International Centre of Supernovae, Yunnan Key Laboratory, Kunming 650216, P. R. China

⁶INAF–Osservatorio Astronomico di Brera, via Brera, 28, 20159 Milano, Italy

21 February 2025

ABSTRACT

UV-upturn galaxies are characterized by unusually excessive flux in the far-ultraviolet (FUV) band, observed in some elliptical galaxies and the bulges of disk galaxies. We examine UV-upturn galaxies within the semi-analytic model *GABE*, which embeds the formation of extreme horizontal branch (EHB) stars—proposed as key candidates responsible for the UV-upturn phenomenon. We have analyzed all related physical processes, including stellar evolution, initial mass functions (IMFs), dust attenuation, galaxy age, metallicity, and binary fractions, in an effort to determine which processes play significant roles. Our findings reveal two categories of UV-upturn galaxies in the semi-analytic model, each with distinct formation channels: old metal-rich quenched elliptical galaxies, which are intrinsic UV-upturn galaxies induced by EHB stars within their old stellar populations, and dusty star-forming galaxies, which are relatively young and may also be photometrically identified as UV-upturn galaxies when accounting for dust attenuation. Dust attenuation contributes to 20% – 60% of the UV-upturn galaxies, depending on the specific dust attenuation models adopted. With the binary star formation model of EHB stars, both of these formation channels exhibit strong preferences for high stellar metallicity. The high-mass end slope of the IMFs is found to have a marginal effect, indicating that a universal IMF is adequate for studying the UV-upturn phenomenon.

Key words: galaxies: elliptical and lenticular – ultraviolet; galaxies – stars: binaries – stars: horizontal branch

1 INTRODUCTION

The “UV upturn” or “UV excess” is an unusual phenomenon characterized by excessive far-ultraviolet (FUV) flux observed in some elliptical galaxies and the central bulge of some spiral galaxies, such as M31 (e.g. Rosenfield et al. 2012). This phenomenon was discovered with the first FUV observations by the Orbiting Astronomical Observatory 2 (OAO-2; Code 1969; Code & Welch 1979). Early imaging and spectroscopic studies found that the UV excess is extended (e.g. Deharveng et al. 1985; Welch 1982), but lacking association with massive stars (e.g. King et al. 1992; Bertola et al. 1995) or star formation activities (e.g. O’Connell et al. 1992). Further spectral and photometric analyses have shown that white dwarfs alone cannot account for the entire UV-upturn phenomenon (Werle et al.

2020). These observations collectively suggest that the UV excess is not due to young massive stars, but rather originates from old stellar populations other than white dwarfs. Additionally, studies examining UV-upturn galaxies across various low-redshift environments have found no dependence of UV excess on cluster environment, group multiplicity, or satellite velocity dispersion. This suggests that the UV upturn is driven by processes internal to the galaxies themselves (e.g. Yi et al. 2011; Loubser & Sánchez-Blázquez 2011; Boissier et al. 2018; Ali et al. 2018c, 2019; Phillipps et al. 2020).

Studies of galaxies at higher redshifts generally report a moderate to negligible evolution in UV excess over redshifts from $z \sim 0$ up to $z \sim 0.6 - 0.7$ (e.g. Brown et al. 1998, 2000a, 2003; Ree et al. 2007; Donahue et al. 2010; Boissier et al. 2018; Atlee et al. 2009). Beyond this range, the occurrence of the UV-upturn phenomenon declines rapidly (e.g. Le Cras et al. 2016; Ali et al. 2018b,c, 2021; De Propriis et al. 2022; Ali et al. 2024). Although Le Cras et al. (2016) observed the near disappearance of the UV-upturn phenomenon at $z \sim 1$ in a sample of massive galaxies from the

* E-mail: jiangzhen@nao.cas.cn

† E-mail: cli2015@tsinghua.edu.cn

Baryon Oscillation Spectroscopic Survey (BOSS, Dawson et al. 2013), Lonoce et al. (2020) reported detecting UV-upturn galaxies at $z \sim 1.4$ in the Cosmological Evolution Survey (COSMOS) field. In this context, the UV-line indices could only be explained after considering an old, UV-bright stellar population, consistent with the previously identified origin from old populations in low-redshift UV-upturn galaxies.

Another well-known observational result is the metallicity dependence of the UV upturn, originally identified by Burstein et al. (1988) through the study of the International Ultraviolet Explorer (IUE) spectra of 24 quiescent early-type galaxies (ETGs). They found that the FUV-V color of these galaxies became bluer with a higher Lick Mg_2 absorption index, indicating higher metallicity. While this correlation has been re-evaluated with subsequent observational data, early studies reported either no correlation (e.g. Ohl et al. 1998; Deharveng et al. 2002; Rich et al. 2005) or only modest correlations (e.g. Boselli et al. 2005; Donas et al. 2007). More recent research has accumulated evidence supporting this correlation. For example, Bureau et al. (2011) demonstrated strong correlations between the FUV-V and FUV-NUV colors and the integrated Mgb index in nearby ETGs with purely old stellar populations using FUV/NUV photometry from GALEX (Martin et al. 2005) and integral field spectroscopy from SAURON (Emsellem et al. 2004). Additionally, Jeong et al. (2012) found that the global correlation of the FUV excess with metallicity also applies at a local level. Furthermore, Carter et al. (2011) observed that the strength of the UV upturn correlates more strongly with $[\alpha/Fe]$ than with $[Z/Fe]$. The correlation between FUV-NUV and FUV-optical colors with metallicity is also observed in rich galaxy clusters in the local Universe, such as Coma (Smith et al. 2012) and Virgo (Akhil et al. 2024).

Theoretically, extreme horizontal branch (EHB) stars and their hot post-HB descendants, including post-early asymptotic giant branch (AGB) stars and AGB-manqué stars, have been proposed as key candidates responsible for the UV excess in old, long-lived stellar populations (Greggio & Renzini 1990, 1999). EHB stars are core-helium-burning stars characterized by extremely thin hydrogen envelopes ($M_{env} < 0.02 M_{\odot}$), with temperatures $T_e \sim 25,000$ K and masses of approximately $0.5 M_{\odot}$. They fall below the main sequence of massive stars on the Hertzsprung-Russell (H-R) diagram and are particularly energetic in the FUV band. Given that 10 – 20% of evolving stars pass through the EHB channels, the observed FUV luminosities can be reasonably explained by EHB stars (Greggio & Renzini 1999; Brown et al. 1995). The detection of EHB and post-EHB stars in M32 by the Hubble Space Telescope provided direct evidence for the EHB origin of the UV excess (Brown et al. 2000b, 2008); for a comprehensive review, see O’Connell (1999).

Although the EHB origin has become a consensus among the community, the specific physical mechanisms driving the formation of the thin hydrogen envelope—critical for EHB star formation—remain unclear (Iben & Rood 1970; Dorman 1992). Several theoretical models have been proposed to explain the formation of this thin envelope. For instance, the “metal-poor single star model” interprets EHB stars as products of the metal-poor tail of a stellar population with a wide metallicity distribution (Lee 1994; Park & Lee 1997). However, this model requires the stellar population to be extremely old (18 – 20 Gyr), even older than the age of the Universe. In contrast, the “metal-rich single star model” assumes that EHB stars originate from metal-rich stars that undergo significant envelope loss near the tip of the red giant branch (RGB, e.g. Bressan et al. 1994; Dorman et al. 1995; D’Cruz et al. 1996; Yi et al. 1997; Maraston 2005). This model posits a relatively

large mass-loss rate that increases with metallicity during the RGB phase in order to reduce the envelope mass (Yi et al. 1998). A more recent model, the “He-rich single star model” (e.g. Chung et al. 2011, 2017), suggests that EHB stars form from subpopulations with high initial helium abundances, which possess high mean molecular masses and short lifetimes, leading to low turn-over masses and thin envelopes. Additionally, a higher abundance of helium results in HB stars burning more of their hydrogen envelope during their HB phase (Horch et al. 1992; Dorman et al. 1995). Both the metal-rich and He-rich single star models predict a relatively strong evolution of the UV excess phenomenon with both metallicity and age of the stellar population, which can account for the observed correlation noted by Burstein et al. (1988) as well as the redshift evolution described by Ali et al. (2021, 2024). The He-rich model effectively reproduces the He-rich EHB subpopulations observed in globular clusters (GCs) (Chung et al. 2011; Peacock et al. 2018), while the increased mass-loss rate during the RGB phase required by the metal-rich model has not been observed in star clusters (Miglio et al. 2012; McDonald & Zijlstra 2015; Williams et al. 2018). Given these observations, the He-rich model is favored over the metal-rich model, assuming that the EHB stars in star clusters share the same origin as those in ETGs (Goudfrooij 2018).

In contrast to the single star models, the “binary star model” considers various binary interactions as the formation mechanism for EHB stars. An EHB star may form after the common-envelope phase of a close binary system if helium is subsequently ignited in the star’s core. Conversely, if mass transfer remains dynamically stable, the star’s envelope will be stripped via stable Roche lobe overflow (RLOF), resulting in a remnant core with a long orbital period that may also evolve into an EHB star if helium in the core is ignited. Furthermore, a single EHB star can originate as the merger remnant of two helium white dwarfs, provided the total mass is less than the Chandrasekhar limit (Webbink 1984; Iben & Tutukov 1986; Han 1998). Han et al. (2002, 2003) meticulously examined all these formation channels and conducted a binary population synthesis study of EHB stars, successfully explaining the observed EHB star distributions without making specific assumptions regarding mass-loss rates and He abundance. Han et al. (2007) further developed an evolutionary population synthesis (EPS) model. In this model, for old stellar populations, the FUV-NUV color decreases substantially with age, while the FUV- r color exhibits a relatively weak correlation with age, consistent with the observed weak evolution of the FUV- r color at $z < 0.6$. Although only solar metallicity was considered, the authors argued that the UV excess phenomenon should not depend strongly on metallicity, as the mass transfer processes related to the formation of EHB stars are primarily influenced by initial orbital parameters rather than metallicity. Consequently, the binary star model predicts a weak or negligible correlation between the FUV- r color and metallicity, which contradicts previous observational studies.¹

In previous studies, the evolution and correlation of the UV-upturn phenomenon were generally derived for simple stellar populations (SSPs), where stars were assumed to form through a singular starburst (e.g. Hernández-Pérez & Bruzual 2013, 2014), composite stellar populations (CSPs) comprising two SSPs (e.g. Han et al. 2007), or CSPs that incorporated chemical evolution histories (e.g. Ali et al. 2021). Assumptions and simplifications were applied to

¹ We note that the metallicity dependence of the UV upturn in binary star models is revisited in this work, leading to somewhat different conclusions. Details can be found in subsection 4.2.

the star formation histories (SFHs) of ETGs. In this work, we examine the formation and evolution of the UV-upturn phenomenon at galactic scales (as opposed to stellar population scales), particularly including variations in SFHs by embedding the formation model of EHB stars within a cosmological framework provided by semi-analytic models (SAMs). In SAMs, the SFHs of galaxies are generated self-consistently through a series of galactic physical processes described by simplified models or empirical relations. Combined with N-body merger trees of dark matter haloes and tracking the formation and evolution of galaxies within these haloes, SAMs have successfully reproduced a substantial amount of observational data at both low and high redshifts (e.g. White & Frenk 1991; Kauffmann et al. 1999; Croton et al. 2006; De Lucia & Blaizot 2007; Guo et al. 2011; Henriques et al. 2015, 2020). The SAM employed in this study is *GABE* (Galaxy Assembly with Binary Evolution, Jiang et al. 2019), which includes a comprehensive set of galaxy formation recipes, encompassing reionization, gas cooling, star formation, supernova feedback, black hole growth, AGN feedback, galaxy mergers, and more. Notably, the evolution of binary stars, particularly the channels for the formation of EHB stars, is integrated using the *YUNNAN-II* EPS model (Zhang et al. 2010).

In addition, the approach of SAMs enables us to examine the influence of various galactic physical processes on the UV-upturn phenomenon. In particular, we will consider stellar initial mass functions (IMFs) with varying slopes at the high-mass end, dust attenuation curves with varying slopes and UV bump strengths, and the fractions of binary stellar populations and young stellar populations. By incorporating these factors into SAMs and comparing the predicted occurrence rates of UV-upturn galaxies, we are able to determine which of these factors might exert important influences on the identification and formation of UV-upturn galaxies.

The organization of this paper is as follows. In section 2, we briefly introduce the adopted semi-analytic model. In section 3, we demonstrate properties of modeled galaxies, and conduct a thorough examination of related physical processes to assess their influence on the formation of UV-upturn galaxies, including various EPS models, IMFs, dust attenuation, and the joint dependencies. We discuss the dependence of UV upturn in binary star model and the role of dust attenuation in section 4, and summarize our conclusions in section 5.

2 SEMI-ANALYTIC MODEL

We utilize the semi-analytic model (SAM) *GABE* (Galaxy Assembly with Binary Evolution) developed by Jiang et al. (2019) as the basic tool for our study. The *GABE* model is implemented using the Millennium Simulation (Springel et al. 2005), a dark matter-only cosmological simulation which adopts the cosmological parameters ($\Omega_m = 0.25$, $\Omega_b = 0.045$, $\Omega_\Lambda = 0.75$, $n = 1$, $\sigma_8 = 0.9$ and $H_0 = 73 \text{ km s}^{-1} \text{ Mpc}^{-1}$) derived from a combined analysis of the 2dFGRS (Colless et al. 2001) and the first-year WMAP data (Spergel et al. 2003). Dark matter haloes and subhaloes are identified with a friends-of-friends group finder (Davis et al. 1985) and *SUBFIND* (Springel et al. 2001), respectively. The merger trees are constructed by tracing the formation and merger history of each halo and subhalo with the D-Tree algorithm (Jiang et al. 2014), upon which *GABE* is applied. The simulation box size is 685 Mpc, which is large enough to suppress cosmic variance, thereby enabling reliable statistics (Wang et al. 2017). The mass resolution of dark matter particles is $1.2 \times 10^9 M_\odot$, allowing *GABE* to generate a com-

plete galaxy catalogue for galaxies more massive than $\sim 10^9 M_\odot$. Like other SAMs, *GABE* includes a full set of galaxy formation recipes, including reionization, gas cooling, star formation, supernova feedback, black hole growth, AGN feedback, galaxy mergers, etc. As shown in Jiang et al. (2019), *GABE* successfully reproduced the stellar mass function of galaxies as well as the scaling relations of galaxy properties such as metallicity, black hole mass, galaxy size and so on. The reader is referred to Jiang et al. (2019) for further details of the model.

As mentioned, UV excess is observed in ellipticals or galactic bulges. In order to facilitate a more reasonable comparison between model and observation, we only consider the “bulge region” of each model galaxy. The “bulge region” of a galaxy is defined as the area within twice the half-mass radius of the stellar bulge, which is formed mainly through galaxy mergers in *GABE*. Assuming the density profile of the galactic disk to be exponential, we calculate the volume fraction of this bulge region over the whole disk and assign the corresponding fraction of disk component to the bulge. In this way, we will compare different properties of the bulge region of model galaxies with observations, and the model galaxies mentioned hereafter are represented by their bulge regions. Note that a model galaxy defined in this way is naturally a composite of a bulge with or without a disk. The ones without disks are analogous to fully quenched elliptical galaxies in observations, while those with disks can be compared with elliptical galaxies with certain levels of star formation activities or with the bulges of spiral galaxies in observations. We only consider modeled galaxies whose bulge region is more massive than $10^{9.5} M_\odot$.

When a star formation event happens in a galaxy, triggered by disk instability or galaxy merger, a corresponding SSP is generated to record the time and strength of this event. The star formation history (SFH) of the galaxy is constructed by aggregating all SSPs throughout its history. UV and optical magnitudes are then derived for the galaxy by convolving the SFH with the photometric evolution of SSPs provided by the adopted EPS models. For the calculation of magnitudes, it is crucial to include dust attenuation, which will be discussed in detail in subsection 3.4. Compared with previous SAMs, *GABE* for the first time incorporated the modeling of binary star evolution by adopting the *YUNNAN-II*² EPS model (Zhang et al. 2004, 2005, 2010, 2020). This model is constructed based on the rapid binary star evolution (BSE) algorithm of Hurley et al. (2002), which encompasses various binary interactions, such as mass transfer, mass accretion, common-envelope evolution, collisions, supernova kicks, tidal evolution, and angular momentum loss via gravitational waves. More technical details on the *YUNNAN-II* model, including initial distributions and spectral library, are available in Zhang et al. (2020). In Zhang et al. (2010), different formation channels of EHB stars of Han et al. (2002, 2003) were also included by directly integrating the EPS model with those of Han et al. (2007), under the assumption that metallicity does not play an essential role in the formation of EHB stars. Consequently, there are three versions of the *YUNNAN-II* model: the single star version by deactivating all binary interactions (*YII-sin*); the binary version without the formation of EHB stars through double He white dwarfs merger, stable RLOF and common-envelope ejection under the assumption of sub-He core ignition³ (*YII-bin*); and the binary version with all the above binary formation channels of EHB stars

² <http://users.ynao.ac.cn/~zhangfh/>

³ The minimum core mass for helium ignition could be lowered if the mass-loss rate during RGB phase is high enough, which increases the formation

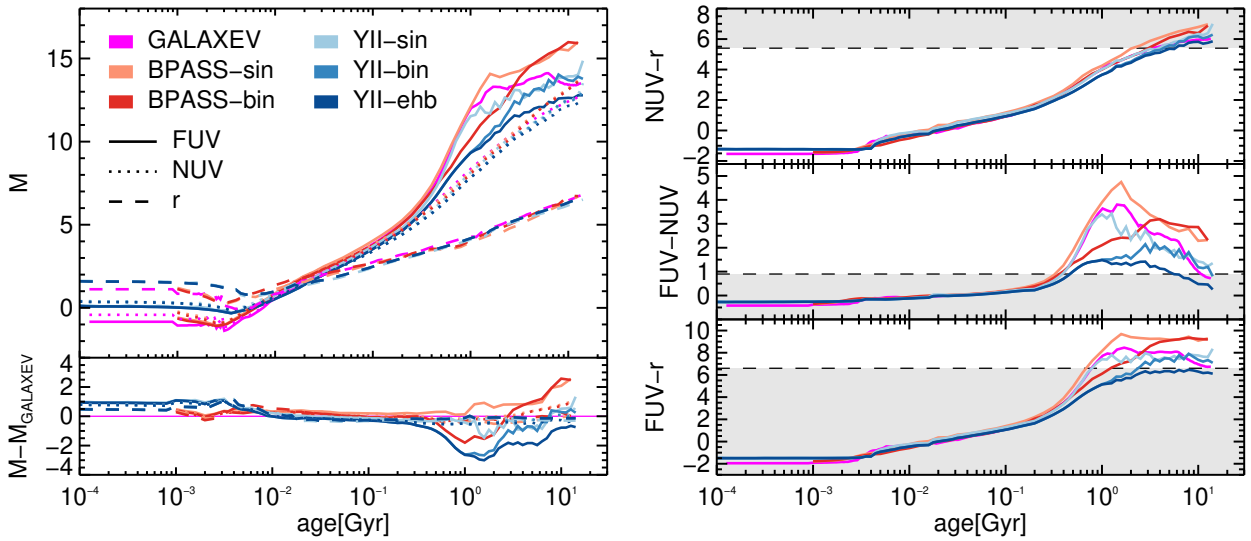


Figure 1. *Left:* Evolution of the FUV, NUV and r band absolute magnitude of a $1 M_{\odot}$ SSP with solar metallicity in different EPS models. For models other than GALAXEV, the relative differences with respect to GALAXEV are shown in the lower panel. The thin magenta horizontal line indicates zero. *Right:* Evolution of NUV- r , FUV-NUV and FUV- r colors for the same models as in the left panel. The shaded regions indicate the colors expected for UV-upturn galaxies.

(*YII-ehb*). The stellar initial mass function (IMF) of Miller & Scalo (1979) is adopted as the fiducial IMF in YUNNAN-II models, but a variety of IMF models will be considered in subsection 3.3.

In addition to YUNNAN-II models, we also consider the EPS model of Binary Population and Spectral Synthesis (BPASS⁴; Eldridge et al. 2008; Eldridge & Stanway 2009; Eldridge et al. 2017), as well as GALAXEV, the commonly-used EPS model of Bruzual & Charlot (2003). The GALAXEV adopts the IMF of Chabrier (2003) and has no formation channels of EHB stars and their descendants. The BPASS model is based on a custom version of the Cambridge stellar evolution code STARS (Eggleton 1971) and the binary evolutionary scheme of Hurley et al. (2002). This model was initially developed to investigate the effects of massive binaries on young stellar populations and has been widely used by both stellar and extragalactic studies (e.g. Blagorodnova et al. 2017; Ma et al. 2016). The properties of old stellar populations were also reevaluated in Stanway & Eldridge (2018), leading to an improved concordance with observed colors and spectral indices in both globular clusters and quiescent galaxies. However, a discussion on the UV-upturn phenomena in these models was absent, and the formation channels of EHB stars through binary interactions of Han et al. (2002, 2003) were not explicitly incorporated. The BPASS v2.2 model provides predictions for both single and binary populations with various IMFs.

3 RESULTS

3.1 Colors of simple stellar populations

We first examine the magnitudes and color indices in UV and optical bands for Simple Stellar Populations (SSPs) across different Evolutionary Population Synthesis (EPS) models. The left panels in

Figure 1 illustrate the evolution of magnitude in the Far UV (FUV), Near UV (NUV), and r band for a $1 M_{\odot}$ SSP with solar metallicity ($Z = 0.02$), for all six EPS models. The models show negligible differences in both NUV and r magnitude when stellar age exceeds ~ 0.01 Gyr. In contrast, significant variations among the models are observed in the FUV magnitude for SSPs older than ~ 0.3 Gyr, where *YII-bin* and *YII-ehb* models are more luminous than *YII-sin* and GALAXEV in the FUV band, attributable to the increasing impact of binary interactions. These interactions, such as mass transfer and merger, give rise to hotter stellar objects, predominantly hot subdwarfs and blue stragglers⁵, enhancing the FUV luminosity around 1 Gyr compared to single star scenarios. At ages larger than ~ 3 Gyr, Extreme Horizontal Branch (EHB) stars produced through the three formation channels of Han et al. (2002, 2003) play a more significant role, lowering the FUV magnitude by an additional magnitude, potentially accounting for the UV-upturn phenomenon observed in elliptical galaxies, as discussed in Han et al. (2007). The BPASS models share a similar evolution with that of YUNNAN-II, but are about 1 – 2 magnitudes fainter in the FUV band at large ages. Due to the lack of formation channels of EHB stars of Han et al. (2002, 2003), the single and binary models of BPASS gradually converge with each other at ~ 3 Gyr.

The right panels of Figure 1 illustrate the evolution of NUV- r , FUV-NUV, and FUV- r colors for the same models, along with the UV-upturn classification scheme of Yi et al. (2011), which is $\text{NUV}-r > 5.4$, $\text{FUV}-\text{NUV} < 0.9$, and $\text{FUV}-r < 6.6$, indicated by the dashed lines and shaded regions. Compared to single star models, those incorporating binary interactions consistently produce bluer SSPs. Among the color indices, NUV- r exhibits minimal influence from binary interactions and shows the least variation across different EPS models. This can be attributed to the weak model-

efficiency of EHB stars (D’Cruz et al. 1996; Han et al. 2002). We refer to such mechanism as “sub-He core ignition”.

⁴ <https://bpass.auckland.ac.nz/>

⁵ Blue stragglers are stars lying on the main sequence in the color-magnitude diagram of globular clusters while beyond the turning-point (Sandage 1953). They are believed to be produced from collisions between low-mass stars and mass transfer in close binaries (e.g., Pols & Marinus 1994; Chen & Han 2004; Hurley et al. 2005).

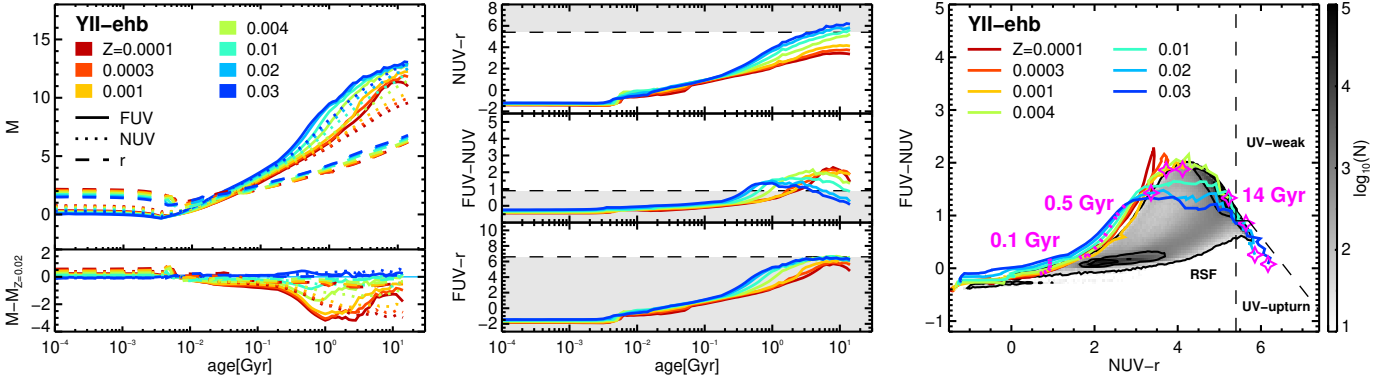


Figure 2. The left two panels are the same as in Fig. 1, but for SSPs with different metallicities in *YII-ehb* model. The right panel shows the evolutionary trajectories of SSPs with different metallicities on the color-color diagram in *YII-ehb* model. Magenta dotted lines are the isochrones and magenta stars mark the evolutionary end points for each trajectories. Gray-filled region shows the number of modeled galaxies without dust attenuation in each cell at $z \sim 0$. Black contours enclose 50%, 80% and 99.8% of all the modeled galaxies respectively outwards. Dashed lines are the divisions of three kinds of galaxies as proposed in [Yi et al. \(2011\)](#): UV-upturn galaxies, UV-weak galaxies, and residual star formation (RSF) galaxies.

dependence of both NUV and r magnitudes observed in the left panels. The other two color indices, both involving FUV, present significant variations among the EPS models for ages exceeding ~ 0.3 Gyr. In these cases, SSPs from single star models rapidly become red, while those from binary models remain blue due to increasing contributions from blue stragglers and EHB stars at 1 Gyr. The *YII-ehb* model presents the bluest colors at large ages, with FUV-NUV progressively becoming bluer after ~ 1 Gyr and FUV- r remaining largely constant. Notably, only the *YII-ehb* model falls into the UV-upturn region when the SSPs are older than ~ 6 Gyr. Other EPS models exhibit relatively weaker FUV flux, thereby failing to meet the criteria for FUV-NUV and FUV- r colors, despite their FUV-NUV colors showing a similar trend towards the blue end at old ages. Furthermore, it is evident that young SSPs are unable to meet the UV-upturn criterion, as their relative flux of NUV over optical is excessively high.

In [Figure 2](#), we examine the dependence of magnitudes and colors on stellar metallicity, focusing solely on the *YII-ehb* model for simplicity and clarity. Examination of other EPS models reveals similar trends. As observed, in all bands, SSPs of higher metallicities are brighter initially but become fainter when the stellar age exceeds ~ 0.01 Gyr. The metallicity dependence at old ages is more pronounced in FUV and NUV than in the r band, with the disparity in UV magnitudes between the most metal-rich and most metal-poor SSPs reaching up to 4 magnitudes, compared to a difference of less than one magnitude in the r band. At late ages, metal-rich SSPs are redder in both NUV- r and FUV- r than metal-poor SSPs. The situation is more complex for FUV-NUV, which increases to a peak before declining again, with the peak color occurring earlier for SSPs of higher metallicities (e.g., $0.6 - 0.7$ Gyr for $Z = 0.03$ and $6 - 7$ Gyr for $Z = 0.0001$). Consequently, only for old metal-rich SSPs with $Z > 0.01$ and ages ≥ 4 Gyr can both the NUV- r and FUV-NUV colors evolve into the UV-upturn region, as indicated by the shaded areas in the middle panel of [Figure 2](#).

Based on these results, we expect the UV-upturn phenomenon to be associated with SSPs of high metallicities and old ages in the *YII-ehb* model. This is more clearly illustrated in the right panel of [Figure 2](#), where the evolution of the *YII-ehb* SSPs is plotted on the FUV-NUV versus NUV- r diagram. The different solid lines indicate the evolutionary trajectories of SSPs with varying metallicities, while magenta dotted lines represent isochrones at 0.1 and 0.5 Gyr.

For comparison, the distribution of all model galaxies *without* dust attenuation is plotted in the background as gray-filled areas. The corresponding black contours outline the star-forming/blue population and quenched/red population. We find that the quenched/red population of galaxies aligns closely with “old” SSPs (> 10 Gyr). Magenta stars denote the endpoints (14 Gyr) of each trajectory, showing a clear dependence on metallicity. Old and metal-rich SSPs exhibit relatively redder NUV- r colors and bluer FUV-NUV colors compared to their metal-poor counterparts, with the most metal-rich SSPs ending right within the UV-upturn region. This further suggests a correlation between the UV-upturn phenomenon and both metallicity and age within the *YII-ehb* model.

3.2 Colors and redshift evolution of model galaxies

[Figure 3](#) displays the distributions of all model galaxies at $z \sim 0$ on the FUV-NUV versus NUV- r color diagram, obtained by adopting different EPS models as indicated. Black contours show galaxy number density, while filled colors depict the mean specific star formation rate (sSFR)⁶ within each cell. For YUNNAN-II and GALAXEV, the fiducial or default IMF is applied, while for BPASS, we use the IMF with a slope of $\Gamma = 1.35$ for both single and binary population models. For comparison, we selected a volume-limited sample of elliptical galaxies with both optical and UV photometry from the NASA-Sloan Atlas (NSA, [Blanton et al. 2005](#)), a local galaxy catalogue constructed from the *Sloan Digital Sky Survey* (SDSS, [York et al. 2000](#)) and *Galaxy Evolution Explorer* (GALEX, [Martin et al. 2005](#)). Our sample comprises 35,336 elliptical galaxies with redshift $0.01 < z < 0.05$, stellar mass $M_* > 10^{9.5} M_\odot$, and Sersic index $n_s > 2.5$. The distribution of this sample is plotted as purple contours, repeated in every panel of [Figure 3](#). In each panel, dashed lines indicate the empirical criteria suggested by [Yi et al. \(2011\)](#) to identify UV-upturn galaxies, which are located in the

⁶ For modeled galaxies with sSFR lower than 10^{-13} yr^{-1} , we set their sSFR to 10^{-13} yr^{-1} . In observations, the uncertainty in measuring sSFR for galaxies with sSFR less than 10^{-13} yr^{-1} is large and not well determined (see Fig. 15 in [Salim et al. 2007](#)). Thus, in our semi-analytic model, although sSFR can be estimated down to 10^{-20} yr^{-1} , we set 10^{-13} yr^{-1} as the lower limit for comparability with observations. In reality, these galaxies represent exhausted systems with almost no star formation.

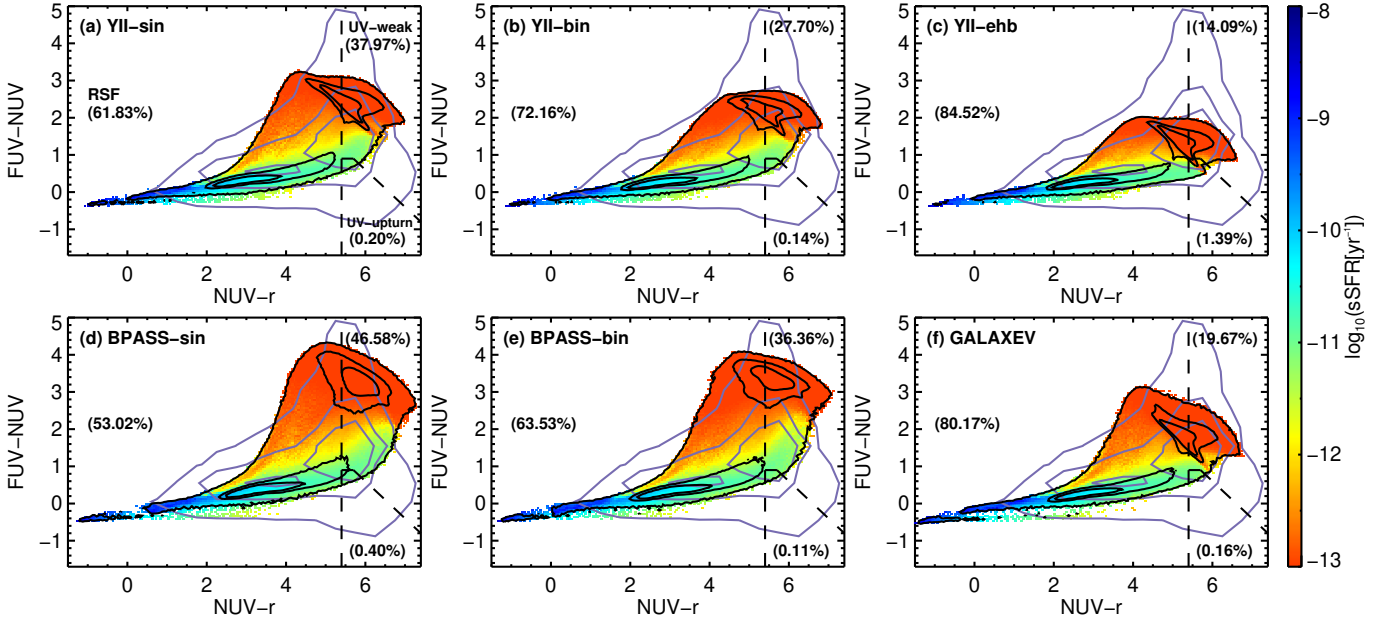


Figure 3. Distributions of model galaxies on the color-color diagram, run with different EPS models. Black contours enclose 50%, 80% and 99.8% of all the modeled galaxies respectively outwards. Filled colors represent the mean specific star formation rate (sSFR) in each cell for cells with more than five galaxies. Dashed lines are the divisions of three kinds of galaxies, with number fractions listed in brackets. Purple contours show the number distributions of galaxies for the observational sample of NSA, enclosing 50%, 80% and 97% respectively outwards.

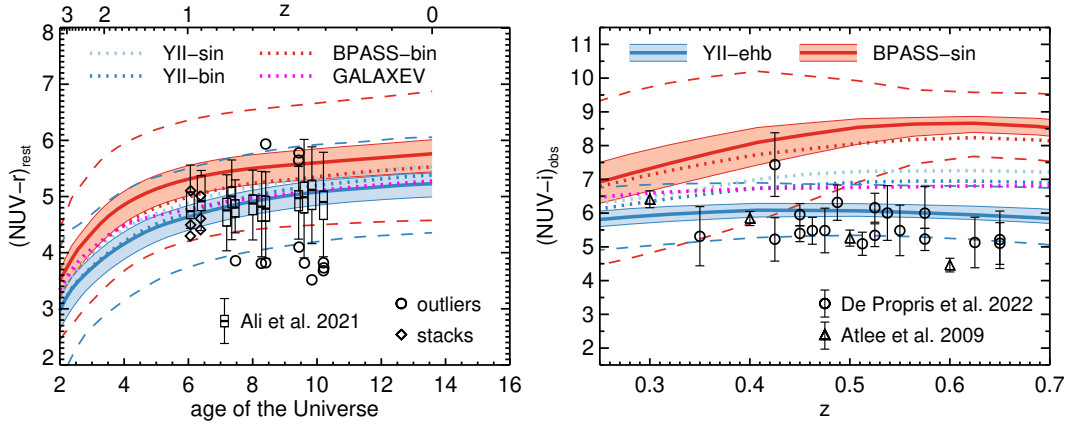


Figure 4. *Left:* Redshift evolution of rest-frame NUV- r colors of modeled quenched galaxies ($\text{sSFR} < 10^{-12} \text{ yr}^{-1}$) run with various EPS models as shown in the legend. Thick solid lines and dotted lines are the median values, and shaded regions indicate the 25% and 75% quartiles. Dashed lines mark the range corresponding to an additional 1.5 times the interquartile range. The *YII-ehb* and *BPASS-sin* models are fully illustrated as thick solid lines with corresponding distributions as the lower and upper limits of model predictions, respectively; and the median values of other EPS models are marked as dotted lines for clarity. Box plots are the observational results of ETGs in 12 clusters in [Ali et al. \(2021\)](#), whose boxes and whiskers share the same definition as our shaded regions and dashed lines, respectively. Circles are observed outliers beyond the whisker range in each cluster, and diamonds are stacks in two clusters at high redshifts. *Right:* The same as the left panel, but for the observed NUV- i colors. Data points are the observational results of field red galaxies of [De Propriis et al. \(2022\)](#) and [Atlee et al. \(2009\)](#), and their error bars illustrate the root mean squares of the mean values from 100 bootstrapping realizations within each magnitude/redshift bin.

lower-right corner of the diagram, with $\text{NUV-}r > 5.4$, $\text{FUV-NUV} < 0.9$, and $\text{FUV-}r < 6.6$.

As can be seen, all models exhibit a bimodal distribution in both color indices, with a clear division between red and blue populations at $\text{NUV-}r \sim 5$, similar to the sample of real galaxies. All models span a similar range in $\text{NUV-}r$, comparable to real galaxies, but the FUV-NUV colors in both red and blue populations are limited to narrower ranges than in the real sample. Consequently, the models lack galaxies with extreme colors, e.g., those with $\text{FUV-NUV} \gtrsim 4$ or $\lesssim -0.5$. Evidently, none of the models can fully reproduce the

distribution of real galaxies in this diagram, indicating the presence of systematic uncertainties within the models. This inconsistency is not unexpected, considering that galaxy colors are not included in the model calibration. We will revisit and discuss this issue in detail in [subsection 4.4](#). In what follows, we will focus on the relative changes in UV and optical colors caused by various physical processes.

The major difference among the models lies in the FUV-NUV color of red populations. The *BPASS* models of both single and binary populations predict redder FUV-NUV colors than the *YUNNAN-*

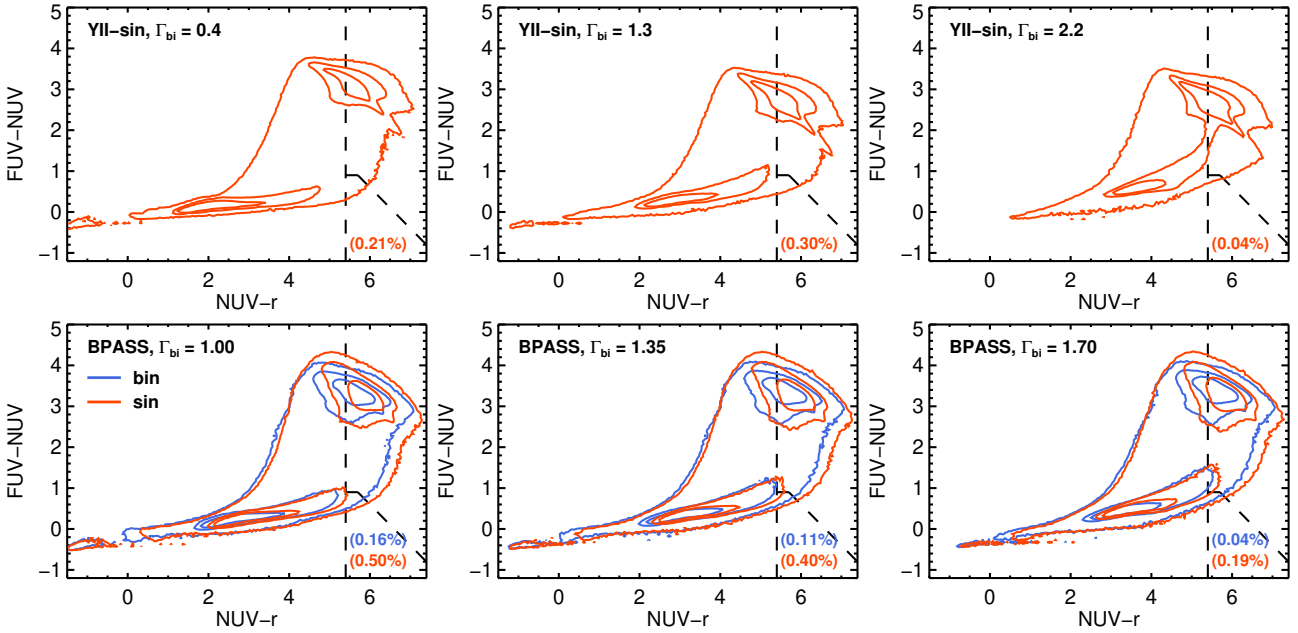


Figure 5. Distributions of modeled galaxies run with *YII-sin* (upper panels) and *BPASS* models (lower panels) with different IMF high-mass end slopes Γ_{bi} , as indicated by different contours. Percentages in brackets are the number fractions of UV-upturn galaxies over all the modeled galaxies.

models. Among other models, the *YII-ehb* model predicts the bluest FUV-NUV colors for the red population. As a result, a tail of the red population in the *YII-ehb* model falls into the UV-upturn region, although the fraction is much smaller than that of UV-upturn galaxies in the real sample due to the aforementioned lack of extreme colors in the models. The fractions of UV-upturn galaxies in the other models are significantly smaller than in the *YII-ehb* case. This echoes the theoretical expectation that the formation of EHB stars through binary interactions can indeed be an efficient way to produce UV excess in elliptical galaxies. Interestingly, in both *YII-bin* and *BPASS*, the single star model and binary model behave similarly in the color-color diagram, with only slight differences in NUV-*r* and almost no difference in FUV-NUV for both red and blue populations.

We now extend the analysis to higher redshifts. The left panel of Figure 4 shows the redshift evolution of the rest-frame NUV-*r* color for quenched galaxies ($\text{sSFR} < 10^{-12} \text{ yr}^{-1}$) in different EPS models. The *YII-ehb* and *BPASS-sin* models yield the bluest and reddest NUV-*r* colors, respectively; therefore, these two models are fully illustrated as thick solid lines with corresponding distributions to indicate the plausible range predicted by different EPS models. The median values of other EPS models are marked as dotted lines for clarity. For comparison, symbols with error bars show ETGs within 12 galaxy clusters at $0.3 < z < 1.0$ from the Hubble Legacy Archive (Ali et al. 2021). While this study does not aim to quantitatively compare our models with observations, it is noteworthy that the model derived with *YII-ehb* agrees quite well with the observational results, in terms of both the median and the scatter of NUV-*r* at a given redshift. However, it is important to note that the differences across different EPS models are comparable to or even smaller than the inherent scatter of galaxies.

In the right panel of Figure 4, we compare the predicted redshift evolution of the "observed" NUV-*i* color of quenched model galaxies with field red galaxies from De Propriis et al. (2022). Following De Propriis et al. (2022), we use the rest-frame FUV-*r* color

from the EPS models as analogues of the observed NUV-*i* colors⁷. As observed, the *YII-ehb* model exhibits marginal agreement with the upper limits of the observational results, whereas other EPS models yield excessively redder colors. The variations of the rest-frame FUV-*r* color among the EPS models are significantly larger than those of the rest-frame NUV-*r* color seen in the left panel, especially at high redshift. This is consistent with what we have seen from Figure 1, where the FUV-involved colors are more powerful than NUV-involved colors in distinguishing different EPS models at old ages. Ali et al. (2021) and De Propriis et al. (2022) suggested that the He-rich single star model provided the best explanation for their observations. Our analysis further suggests that the binary star model *YII-ehb* is also compatible with current observations in terms of the redshift evolution of quenched galaxies at $z \lesssim 1$.

3.3 Influence of stellar initial mass function

The intensity of the UV-upturn phenomenon should, in principle, depend on the high-mass end of the adopted stellar initial mass function (IMF), which determines the fraction of stars more massive than $\sim 0.6 M_{\odot}$, including the progenitors of EHB stars ($0.8 \lesssim m_1 \lesssim 5 M_{\odot}$, Han et al. 2002; Clausen et al. 2012). To investigate this effect, we adopt the "bimodal" IMF form (Vazdekis et al. 1996) to describe IMFs with different slopes at the high-mass end:

$$\Phi(\log_{10}(m_1)) \propto \begin{cases} (m_1/0.6)^{-\Gamma_{\text{bi}}} & (\text{for } m_1 > 0.6 M_{\odot}) \\ p(m_1) & (\text{for } 0.2 \leq m_1 \leq 0.6 M_{\odot}), \\ 1 & (\text{for } m_1 < 0.2 M_{\odot}) \end{cases} \quad (1)$$

⁷ We find the measured NUV-*i* colors are in fact $\sim 1 - 2$ bluer than the rest-frame FUV-*r* colors due to the broader bandwidth of the NUV band (Morrissey et al. 2005). We have corrected this effect for each modeled galaxy according to its redshift and mean mass-weighted age and metallicity, by utilizing spectra of each EPS model.

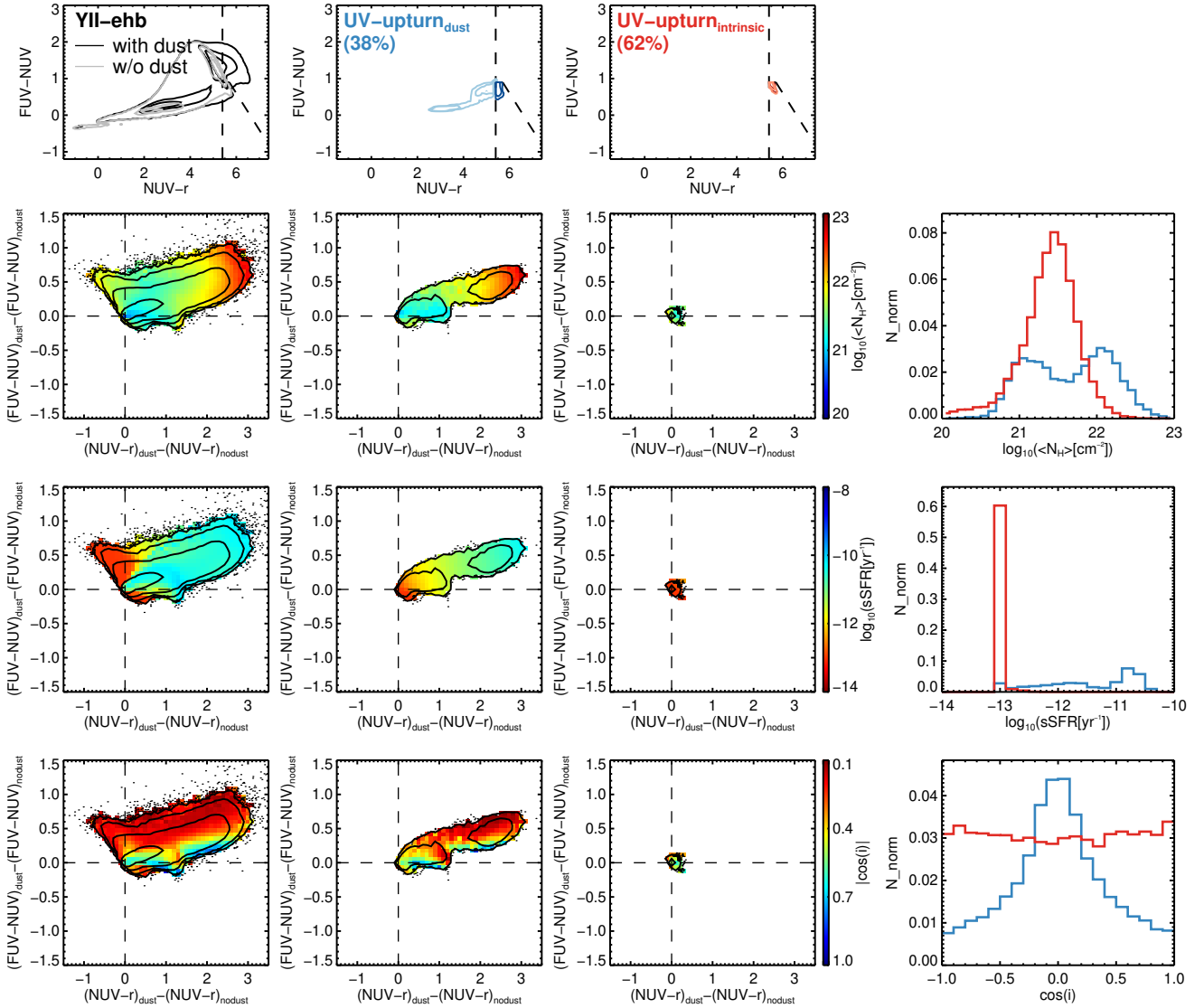


Figure 6. Top panels: Distributions of all modeled galaxies (black), UV-upturn_{dust} galaxies (blue) and UV-upturn_{intrinsic} galaxies (red) on the color-color diagram, by using *YII-ehb* model. Dark/light contours show the ones with/without dust attenuation. Lower panels: Distributions of corresponding reddenings for each kind of galaxies. Black contours show number ratios, and filled colors represent mean H column density $\langle N_H \rangle$, sSFR, and inclination angle $|\cos(i)|$ respectively as indicated by color bars. Distributions of these galactic properties are shown in the right column, normalized by the total number of two kinds of UV-upturn galaxies.

where m_1 is the primary mass in unit of M_\odot , Γ_{bi} is the slope for $m_1 > 0.6 M_\odot$, and $p(m_1)$ is a third-degree spline function connecting the low- and high-mass ends. The slope Γ_{bi} is varied within the range $[0.4, 2.2]$ to mostly encompass the slopes estimated by Zhou et al. (2019) for a sample of elliptical galaxies from the MaNGA survey. All IMFs are assumed to be truncated below $0.1 M_\odot$ and above $100 M_\odot$, and normalized within the range $[0.1, 100] M_\odot$. With this form, the bimodal IMF of $\Gamma_{bi} = 1.3$ is close to the fiducial IMF adopted in GABE (Miller & Scalo 1979, hereafter MS79) at masses up to $\sim 10 M_\odot$ and the commonly-used IMF of Chabrier (2003) at all masses. We have also repeated our analysis using IMFs other than the bimodal IMFs, as well as single power-law IMFs ($\Phi(\log_{10}(m_1)) \propto m_1^{-\Gamma_{si}}$), including the IMF of Salpeter (1955). We find that the specific form of IMFs does not influence our conclusion. Therefore, we only present results from the bimodal IMFs for clarity. A uniform mass-ratio distribution of the secondary and the primary mass (m_2/m_1) is assumed

(Mazeh et al. 1992; Goldberg & Mazeh 1994), as the same in the fiducial YUNNAN-II models.

The implementation of various IMFs for *YII-bin* and *YII-ehb* is not trivial, and the resulting magnitudes are extremely sensitive to model parameters (e.g. Greggio & Renzini 1990; Dorman et al. 1995; Han et al. 2002). Thus, for YUNNAN-II, we explore the effect of IMF variation only for the models of *YII-sin*. In BPASS v2.2, a variety of broken power-law IMFs are available for both single and binary populations (Stanway & Eldridge 2018, see their Tab. 1), which share a similar form with Equation 1 but with marginally steeper slopes at the low-mass end. To be consistent with YUNNAN-II models, we use BPASS data with upper mass cut-offs of $100 M_\odot$. In this way, we have $\Gamma_{bi} = 1.0, 1.35, 1.7$ for both single and binary models from BPASS, as well as a range of $0.4 \leq \Gamma_{bi} \leq 2.2$ for single models from *YII-sin*. With each of the various IMFs and the corresponding EPS models, we run the semi-analytic model code

GABE. The resulting galaxy samples are plotted on the FUV-NUV versus NUV- r diagram in Figure 5.

As Γ_{bi} increases, galaxies within the star-forming sequence become redder in both NUV- r and FUV-NUV color indices, while red population galaxies exhibit minimal change, becoming only slightly bluer in FUV-NUV. This pattern holds true for both the *YII-sin* model and the single model of *BPASS*. The binary model in *BPASS* similarly follows this trend with Γ_{bi} as seen in the single model. The weak dependence of the red population on the initial mass function (IMF) can be attributed to the dominance of long-lived, low-mass stars in these galaxies, which are not substantially affected by changes in the high-mass end slope of the IMF.

When examining the impact on the formation efficiency of UV-upturn galaxies, different behaviors emerge across various evolutionary population synthesis (EPS) models. In the *YII-sin* model, the configuration with $\Gamma_{\text{bi}} = 1.3$ exhibits the highest efficiency. Conversely, in both the single and binary *BPASS* models, top-heavy IMFs (those with lower Γ_{bi}) display higher UV-upturn fractions, with $\Gamma_{\text{bi}} = 1.00$ being the most efficient. These inconsistencies suggest systematic uncertainties related to IMF variations among different EPS models. However, the differences in UV-upturn fractions remain within an order of magnitude. Compared to the influence of extreme horizontal branch (EHB) stars, variations in the IMF appear to have a secondary effect on the formation of UV-upturn galaxies. This suggests that a universal IMF should suffice for investigating the UV-upturn phenomenon.

3.4 Influence of dust attenuation

In our analysis thus far, we have not discussed the effects of dust attenuation, which can absorb and scatter UV and optical light, significantly altering galaxy colors and potentially leading to the incorrect identification of UV-upturn galaxies. To incorporate dust attenuation, GABE uses the model proposed by De Lucia & Blaizot (2007), which considers the reddening effects of both the diffuse interstellar medium (ISM) and birth clouds around young stars. For the ISM, reddening is modeled with a "slab" geometry as described by Devriendt et al. (1999), while the reddening of birth clouds follows the model from Charlot & Fall (2000) and De Lucia & Blaizot (2007). For more comprehensive details on the dust attenuation model, readers are referred to De Lucia & Blaizot (2007) and the references therein. Essentially, the attenuation at a given wavelength for both the ISM and birth clouds is related to the mean optical depth for a face-on average disk, τ_{λ} , which depends on the chosen dust attenuation curve (A_{λ}), gas metallicity (Z_{g}), and mean hydrogen column density ($\langle N_{\text{H}} \rangle$). Additionally, ISM reddening depends on the dust albedo (Mathis et al. 1983) and the inclination angle of the disk ($\cos(i)$), defined as the angle between the direction of the spin of the gaseous disk and the line of sight, assumed to be along the third axis of the N-body simulation.

The impact of dust attenuation is illustrated in the top-left panel of Figure 6, which compares the color-color diagrams of model galaxies with and without dust attenuation. The lower panels in the leftmost column show the distribution of changes in the two color indices due to dust attenuation, color-coded by $\langle N_{\text{H}} \rangle$, sSFR, and $|\cos(i)|$. For simplicity and clarity, we present only the results for the *YII-ehb* model, noting that other EPS models yield similar outcomes. As demonstrated, dust attenuation generally causes model galaxies to appear redder in both FUV-NUV and NUV- r colors, with greater reddening associated with higher values of $\langle N_{\text{H}} \rangle$, sSFR, and inclination angle. To assess the importance of dust attenuation in identifying UV-upturn galaxies, we divide all UV-upturn galaxies

Table 1. Parameters of dust attenuation curves. The parameter $B \equiv A_{\text{bump}}/A_{2175}$ is the fraction of UV bump over the total extinction at 2175 Å, as defined in Salim & Narayanan (2020).

Model	slope δ	bump amplitude E_{b}	Description
M83	-	-	Mathis et al. (1983), fiducial
E130	0.0	13.0	corresponding to $B = 0.6$
E035	0.0	3.5	$B = 0.3$, Milky Way/LMC
E000	0.0	0.0	$B = 0.0$, Calzetti00
Dm06	-0.6	1.99	$E_{\text{b}} = -1.9\delta + 0.85$
D00	0.0	0.85	(Kriek & Conroy 2013)
Dp03	+0.3	0.28	

into two groups: UV-upturn_{intrinsic}, which are intrinsic UV-upturn galaxies that remain in the UV-upturn region after accounting for dust attenuation, and UV-upturn_{dust}, which includes galaxies that enter the UV-upturn region only after accounting for dust attenuation.

The second and third columns of Figure 6 show color-color diagrams and color change distributions for the two categories, while the rightmost column displays histograms of the parameters used to color-code the distributions of color changes. The UV-upturn_{intrinsic} group contains 62% of the UV-upturn galaxies, primarily quenched galaxies with minimal star formation and intermediate $\langle N_{\text{H}} \rangle$. Galaxies in the UV-upturn_{dust} group which consists of 38% of the UV-upturn sample are mainly star-forming, spanning a wide range of sSFR, exhibiting a bimodal distribution in $\langle N_{\text{H}} \rangle$, and a narrow inclination angle range centered at $i = 90^\circ$. The subset with higher $\langle N_{\text{H}} \rangle$ and sSFR experiences more significant reddening, thus shifting from the star-forming sequence into the UV-upturn region. The other subset, nearly quenched with low sSFR, also enters the UV-upturn region, although their reddening is moderate. In addition, we notice that approximately one-fifth of intrinsic UV-upturn galaxies relocate outside the UV-upturn region when dust attenuation is taken into account. Most of these are quenched disk galaxies. Unlike their elliptical counterparts, these quenched disk galaxies are more susceptible to the effects of dust attenuation and may exit the UV-upturn region if their FUV-NUV color becomes excessively red.

By default GABE adopts the attenuation curve of Mathis et al. (1983, M83 hereafter), an average observational relation of stars in the Milky Way (Savage & Mathis 1979), thus exhibiting a noticeable bump at 2175 Å and a relatively steep slope in UV, typical of attenuation curves in Milky Way (Salim & Narayanan 2020). However, previous studies of local galaxies have revealed a wide range of UV slope and UV bump strength (see Salim & Narayanan 2020, for a review). The FUV and NUV magnitudes are expected to be modified differently by attenuation curves of different slopes and UV bumps. To evaluate this effect, we adopt the parameterized formula proposed by Noll et al. (2009b) to describe various dust attenuation curves:

$$A_{\lambda} = \frac{A_{\text{V}}}{4.05} (k'_{\lambda} + D_{\lambda}) \left(\frac{\lambda}{\lambda_{\text{V}}} \right)^{\delta}, \quad (2)$$

where k'_{λ} is the bumpless attenuation curve obtained from local starburst galaxies by Calzetti et al. (2000), hereafter Calzetti00, and D_{λ} is a Lorentzian-like Drude profile to parameterize the UV bump,

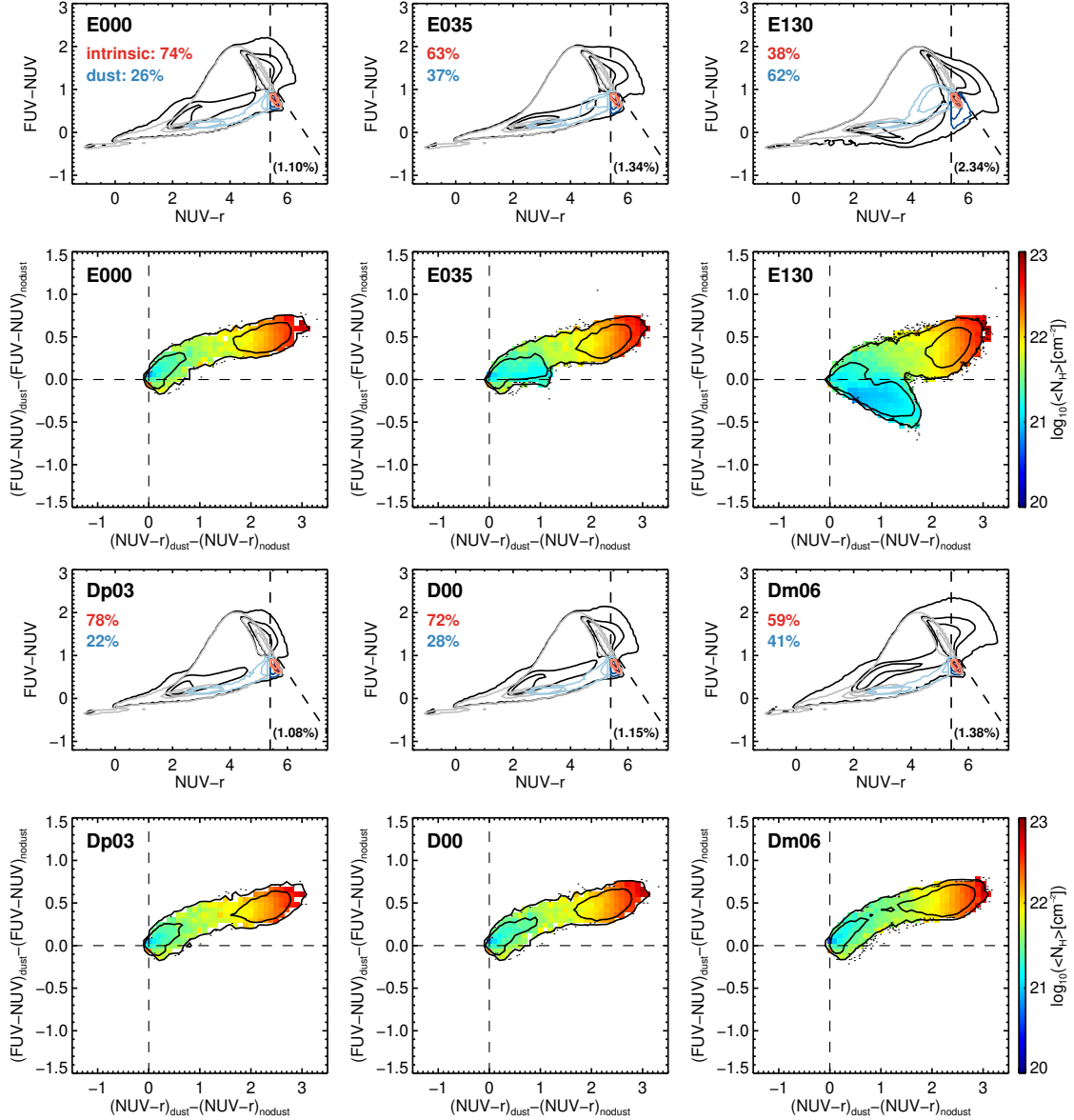


Figure 7. The same as the top row and second column in Figure 6, but for modeled galaxies with different dust attenuation curves as parameterized in Table 1.

given by

$$D_\lambda = \frac{E_b (\lambda \Delta \lambda)^2}{(\lambda^2 - \lambda_0^2)^2 + (\lambda \Delta \lambda)^2} \quad (3)$$

There are four parameters in this parameterization: the slope δ accounts for additional wavelength dependence that diverges from the Calzetti00 curve; E_b , λ_0 and $\Delta \lambda$ denote the amplitude, central wavelength, and full width at half maximum (FWHM) of the UV bump, respectively (Fitzpatrick & Massa 1990). The latter two parameters are set to average values, specifically $\lambda_0 = 2175 \text{ \AA}$ and $\Delta \lambda = 350 \text{ \AA}$ (Noll et al. 2009a; Seaton 1979; Kriek & Conroy 2013), and we investigate the parameter space of the slope δ and the UV bump amplitude E_b . We consider two sets of models of dust attenuation curves with varying parameters δ and E_b as listed in Table 1. The first set is aimed to isolate the effects of UV bump strength, with a fixed slope of $\delta = 0$ but three different values of E_b . The sec-

ond set of models are assumed to follow the observed relation of $E_b = -1.9\delta + 0.85$ from Kriek & Conroy (2013).

Figure 7 presents the color-color diagram and illustrates how model galaxies' colors change with different dust attenuation curves. For each model, the upper panel shows the color-color diagram, with contours in black, red, and blue representing all model galaxies and specifically those in the UV-upturn_{intrinsic} (red) and UV-upturn_{dust} (blue) groups, while the lower panel highlights the shifts in two color indices of UV-upturn_{dust} galaxies, with changes color-coded according to $\langle N_H \rangle$. The percentages in black brackets indicate the ratio of UV-upturn galaxies to the total modeled galaxies, whereas the red and blue percentages denote the proportions of UV-upturn_{intrinsic} and UV-upturn_{dust} galaxies within the UV-upturn category, respectively. When comparing the E000, E035, and E130 models, we observe that the proportion of UV-upturn galaxies rises as the UV bump's strength increases, a trend primarily driven by UV-upturn_{dust} galaxies. This effect is most evident in the E130 model, where the influence of the UV bump leads some green val-

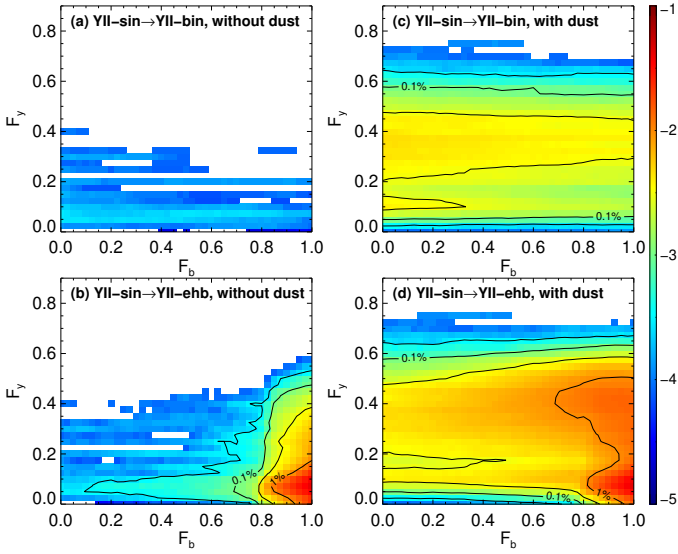


Figure 8. Filled colors in each cell indicate fractions of UV-upturn galaxies ($F_{\text{UV-upturn}}$) as a function of binary mass fraction (F_b) and young fraction (F_y). The latter one is defined as the mass fraction of SSPs which have mass-weighted age younger than 9 Gyr. Cell size is 0.025×0.025 , and only cells with more than 5 galaxies are presented. Contours correspond to the 0.03%, 0.1%, 0.3% and 1% of $F_{\text{UV-upturn}}$. Binary interactions without the formation of EHB stars are shown in the upper panels, and ones with EHB stars are in the bottom panels. Results without dust attenuation are in the left column, and ones with dust are in the right column.

ley galaxies to exhibit bluer FUV-NUV and redder NUV- r colors. Consequently, these galaxies shift towards the lower-right corner of the color-color diagram along the quenched sequence, eventually reaching the UV-upturn region. In contrasting the Dp03, D00, and Dm06 models, where UV bumps are relatively weak, we find that steeper attenuation curves result in greater reddening of both NUV- r and FUV-NUV colors. This alteration makes it easier for star-forming galaxies to transition into the UV-upturn region.

While elliptical galaxies were usually thought to be dust-free, recent studies suggest that residual star formation (RSF) and associated dust attenuation are not uncommon within these galaxies. Kaviraj et al. (2007) found that approximately 30% of ETGs exhibit UV-to-optical colors indicative of some degree of RSF activity occurring within the last Gyr. Additionally, Vazdekis et al. (2016) noted that young stellar populations with ages between 0.1 and 0.5 Gyr contribute mass fractions of 0.1% to 0.5% to massive ETGs, based on their analysis of UV colors and line strengths. Similarly, Salvador-Rusiñol et al. (2020) reported that RSF is prevalent in massive ETGs, with an average mass fraction of around 0.5% in young stars formed within the last 2 Gyr. Notably, Werle et al. (2020) detected young stellar components in 17.5% of the UV-upturn galaxies defined by Yi et al. (2011), which aligns closely with our lower limit in this study. A more in-depth discussion of the role of dust attenuation in the context of UV-upturn galaxies can be found in subsection 4.3.

3.5 Joint dependence on F_b , F_y , Z_* and dust

In the previous subsections, we explored how UV-upturn galaxies are influenced by stellar evolution, which is described through the photometric evolution of SSPs derived from EPS models, as well as by dust attenuation. These are the two primary physical processes

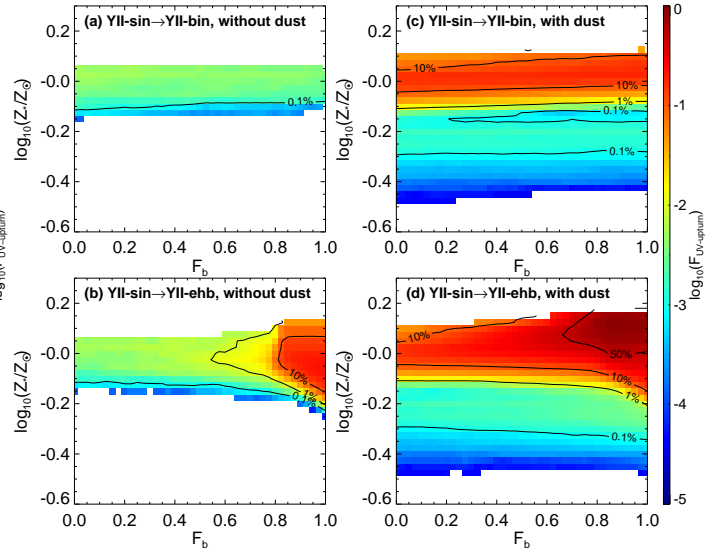


Figure 9. The same as in Fig. 8, but as a function of binary mass fraction (F_b) and stellar metallicity (Z_*). Contours correspond to the 0.1%, 1%, 10% and 50% of $F_{\text{UV-upturn}}$.

involved in calculating magnitudes for galaxies in semi-analytical models. We will now focus on the fiducial YUNNAN-II models and the M83 dust attenuation curve to further examine the dependence on various galaxy properties, including the fraction of binary populations (F_b), the fraction of young populations (F_y), and stellar metallicity (Z_*), considering both scenarios with and without dust attenuation. Here, F_b is defined as the mass fraction of binary populations relative to the total stellar population, while F_y refers to the mass fraction of SSPs with a mass-weighted age younger than 9 Gyr. It is important to note that using an alternative criterion for F_y only affects the detailed scale of the figures and does not change our overall conclusions.

Figure 8 illustrates the distributions of $F_{\text{UV-upturn}}$, defined as the proportion of UV-upturn galaxies corresponding to specific values of F_b and F_y , plotted on the F_y versus F_b plane. The upper panels show models of binary interactions that exclude the formation of extreme horizontal branch (EHB) stars. In these models, varying F_b from 0 to 1 transitions from the *YII-sin* model to the *YII-bin* model by progressively incorporating a F_b fraction of binary populations. In contrast, the lower panels present models that include EHB stars, transitioning from the *YII-sin* model to the *YII-ehb* model. Results without dust attenuation are shown in the left column, where we find that a significant population of UV-upturn galaxies can form only when including binary interactions with EHB stars within old SSPs. Results incorporating dust attenuation are displayed in the right column, revealing a notably larger fraction of UV-upturn galaxies compared to the left panels. Similar to the no-dust scenario, EHB stars contribute to the peak observed around $F_b > 0.8$ and $F_y \sim 0.1$, representing the UV-upturn phenomenon in nearly fully quenched galaxies. Additionally, dust attenuation creates a stripe corresponding to a roughly constant young fraction of $F_y \sim 0.4$, which signifies star-forming galaxies. The influence of EHB stars within old SSPs is evident in both the region representing star-forming galaxies and that of quenched galaxies.

Figure 9 further explores the joint dependence on F_b and stellar metallicity Z_* . Notably, there is a strong preference for high stellar metallicity in both categories of UV-upturn galaxies: those

formed through binary interactions with EHB stars and those resulting from dust attenuation. This finding is consistent with our expectations derived from analyzing SSPs in the *YII-ehb* model. As discussed in subsection 3.1, only the most metal-rich SSPs with $Z > 0.01$ can evolve into the UV-upturn region after approximately 4 Gyr. In contrast, the latter preference emerges from the complex interactions of star formation activities integrated into semi-analytical and dust attenuation models. In the most extreme case, over 80% of galaxies with $F_b > 0.7$ and $\log_{10}(Z_*/Z_\odot) \sim 0.1$ in panel (d) are classified as UV-upturn galaxies, despite the relatively small absolute number of such metal-rich galaxies. This strong preference for high stellar metallicity accounts for the observed correlation between the UV-upturn phenomenon and metallicities (e.g. Carter et al. 2011; Smith et al. 2012; Akhil et al. 2024). Specifically, we find that the mean stellar metallicities of UV-weak and RSF galaxies in the models are approximately 0.15 to 0.2 dex lower than those of UV-upturn galaxies. This aligns well with the observed metallicity differences between UV-upturn and UV-weak regions, as reported in Jeong et al. (2012).

4 DISCUSSION

4.1 Definition of “UV-upturn”

The primary prediction of the “binary star model” (Han et al. 2007) was that the UV-upturn phenomenon exhibits only a weak dependence on the age and metallicity of stellar populations. However, upon revisiting the binary star model within a cosmological context, we find that this prediction requires more nuanced consideration. In this work, we find that binary star model exhibits a strong dependence on both the age and metallicity of stellar population. This discrepancy with Han et al. (2007) is actually mostly attributed to our different definition of “UV-upturn”.

In fact, the definition or measurement of the UV-upturn phenomenon varies from one paper to another. The relatively stringent photometric definition of UV-upturn galaxies of Yi et al. (2011) has been adopted in some observational (e.g. Jeong et al. 2012; Petty et al. 2013; Boissier et al. 2018) and theoretical (e.g. Hernández-Pérez & Bruzual 2014) works to physically select UV-upturn galaxies. While in Han et al. (2007) and many other works, the value of the FUV-*r* color (or other UV-to-optical color) alone was used to quantify the strength of UV excess (e.g. Brown et al. 2003; Donahue et al. 2010; Smith et al. 2012; Phillips et al. 2020; Ali et al. 2021); likewise, in some other works, the FUV-NUV color alone was used (e.g. Loubser & Sánchez-Blázquez 2011; Carter et al. 2011). These choices were made sometimes due to the lack of photometric data at certain wavelengths, or because the sample volume might be largely reduced with additional color criteria. Moreover, observational systematic uncertainties further constrain the power of rather stringent criteria. For example, when the UV-upturn criteria of Yi et al. (2011) were applied to the Coma cluster, Yi et al. (2011) found that none of the 30 brightest elliptical galaxies falls into the UV-upturn region. In contrast, Smith et al. (2012) reported that 14 out of 150 quenched galaxies in the Coma cluster meet the criteria, and this discrepancy was likely due to their different applications of *k*-correction. Furthermore, in some spectroscopic studies of ETGs at high redshift (e.g. Lonoce et al. 2020), line indices were used in SED fitting to ascertain whether a galaxy favors an old stellar population with an upturn contribution, in which case it would be defined as a UV-upturn galaxy. Le Cras et al. (2016) found that the fraction of UV-upturn galaxies

defined in this way was approximately seven times that reported in Yi et al. (2011), as some UV-weak galaxies might also select an upturn SSP if only the line indices’ strength were considered.

Here, we emphasize that the definition or measurement of the UV upturn is crucial when addressing the so-called “UV excess” phenomenon. Theoretical models can exhibit significantly different dependencies on age and metallicity based on the definitions employed. For instance, using the triple color criteria established by Yi et al. (2011), the UV-upturn phenomenon associated with the binary star model shows a strong dependence on both age and stellar metallicity. In contrast, when employing the FUV-*r* color as a measure of the UV upturn’s strength, as done by Han et al. (2007), the dependence on age and metallicity appears relatively weak, as illustrated in the right panel of Figure 1 and middle panel of Figure 2. Conversely, utilizing the FUV-NUV color again suggests a strong dependence on both age and metallicity. Thus, it is essential to clearly define the term “UV-upturn” prior to any discussion, and to ensure consensus on this definition when comparing observations with theoretical models.

4.2 Metallicity dependence

Han et al. (2007) concluded that the formation of extreme horizontal branch (EHB) stars is primarily determined by their initial orbital parameters, with metallicity playing a minimal role in the related mass transfer processes. As a result, the UV-upturn phenomenon was expected to show weak or no correlation with metallicity. However, they also pointed out that metallicity “may affect the properties of the binary population in more subtle ways”. Actually, the total flux of a stellar population consists of contributions not only from EHB stars but also from all other stars. In the *YII-ehb* model, Zhang et al. (2010) incorporated the binary formation channels of EHB stars into the YUNNAN-II model, under the assumption that the formation efficiencies of EHB stars remain unaffected by metallicity. This implies that the absolute contributions of EHB stars are consistent across SSPs with varying metallicities in the *YII-ehb* framework. As illustrated in the middle panels of Figure 2, with this straightforward assumption, UV-upturn phenomenon resulting from binary star model actually exhibits a dependence on metallicity. Adopting the stringent photometric definition of Yi et al. (2011), the dependence is quite strong. Only metal-rich SSPs (with metallicity greater than $0.01Z_\odot$) can reach the UV-upturn region as they age beyond approximately 4 Gyr. In more metal-poor SSPs, the NUV flux from stars other than EHB stars becomes excessively dominant, thereby impeding the fulfillment of the UV-upturn criteria of the NUV-*r* and FUV-NUV colors. In contrast, when utilizing the FUV-*r* color alone as the definition or measurement, the dependence on metallicity becomes much weaker, but not vanished. Consequently, although the formation of EHB stars is not directly influenced by metallicity, the resulting UV-upturn phenomenon is. A similar dependence on metallicity within binary star models was also highlighted by Hernández-Pérez & Bruzual (2014).

4.3 The role of dust attenuation

Although elliptical galaxies are generally found to be quenched and dust-free (e.g. Rettura et al. 2006, 2011; Barber et al. 2007; Ali et al. 2018a), a considerable fraction of ETGs exhibit RSF activities and internal dust extinction (e.g. 27% in Yi et al. 2011, ~ 30% in Kaviraj et al. 2007, ~ 10% in Donas et al. 2007, and 17% in Werle et al. 2020), depending on their different sample selection

criteria and definitions of RSF. With a photometric color selection for relatively red galaxies, such RSF activities cannot be totally removed. As demonstrated in Phillipps et al. (2020), optical red sequence galaxies defined on the $(g-r)$ versus M_r color magnitude diagram are significantly contaminated by RSF galaxies, which can be distinguished by their NUV- r colors. Some of these RSF galaxies are indeed ETGs (e.g. Salim & Rich 2010), while some of them are in fact red spiral galaxies (e.g. Sodr e et al. 2013; Crossett et al. 2014; Mahajan et al. 2020). Even with a relatively strict additional color criterion of NUV- $r > 5.4$, RSF interlopers with strong dust attenuation still exist as discussed in subsection 3.4, and could contribute 20%–60% of the UV-upturn galaxies depending on different dust attenuation models.

In previous studies which focused on UV-upturn phenomenon in old stellar populations, galaxies with RSF activities were treated carefully with many different methods, such as morphological sample selection (Ree et al. 2007), optical to mid-infrared SED fitting (Atlee et al. 2009), emission line features (Loubser & S anchez-Bl azquez 2011), additional star formation sensitive colors (*WISE* W2-W3, Phillipps et al. 2020), and image stacks to marginalize their effect (De Propris et al. 2022). With either method, it is crucial to carefully exclude such RSF interlopers in the discussion of the genuine UV upturn in old stellar populations. In the upper left panels of Figure 8 and Figure 9, we demonstrate that such dust-induced UV-upturn galaxies exhibit a strong preference for young stellar age and high stellar metallicity. Consequently, without a clean sample selection, additional unexpected age and metallicity dependencies could be introduced by these RSF interlopers.

4.4 Limitations and outlook

Utilizing the *YII-ehb* EPS model, our semi-analytic model *GABE* roughly reproduced the observed bimodal color distributions of elliptical galaxies. However, it yields a much narrower FUV-NUV range and an inaccurately positioned star-forming sequence, as shown in Figure 3. Achieving a fully reproduction of the observed color distributions of galaxies remains a difficult challenge in semi-analytic models. Firstly, galaxy colors are generally not used as a model calibrator. Instead, the stellar mass function is the predominant observational result employed for calibration in semi-analytic models (e.g. Guo et al. 2011). Furthermore, scaling relations, such as the supermassive black hole to stellar bulge mass relation, the galaxy size-mass relation, and the metallicity-mass relation, are also ensured during the calibration process. In contrast to these carefully treated galaxy properties, galaxy colors are predictions of semi-analytic models, rather than calibrations. Consequently, semi-analytic models may not perform their best in predicting galaxy colors within the feasible parameter space. Secondly, galaxy colors are highly dependent on the SFHs of galaxies, which are challenging to reproduce self-consistently across various types of galaxies and across different redshifts. Unlike integral galaxy properties such as stellar mass, the star formation rate is differential and sensitive to almost all galactic physical processes, encompassing reionization, hot gas cooling, supernova feedback, galaxy mergers, etc., especially tidal and ram-pressure stripping in satellite galaxies and AGN feedback in massive galaxies. Lastly, numerous physical processes that might influence galaxy colors have not been exquisitely considered in semi-analytic models. As discussed in previous sections, incorporating variations of IMFs, dust attenuation, and binary fractions can significantly alter the distribution of model galaxies on the color-color diagram. The narrower distributions of model galaxies

in comparison to the observed one actually reflect a huge amount of physical processes and their variations in the real Universe which are missed in current semi-analytic models.

In recent years, great efforts have been devoted to better reproduce the SFHs of galaxies, not only on a global scale but also on the satellite scale. For instance, in the GALaxy Evolution and Assembly (GAEA) model, a gas ejection rate that decreases significantly with cosmic time as suggested by hydrodynamical simulations was incorporated to suppress star formation at high redshift (Hirschmann et al. 2016); and a more continuous stripping of hot gas in satellite galaxies was implemented, allowing satellite galaxies to quench in a more gradual way (Xie et al. 2020). In the L-GALAXIES semi-analytic model, the star formation in isolated low-mass galaxies is significantly delayed by a longer reincorporation time of ejected gas (Henriques et al. 2013); the quenching of satellite galaxies is relieved by only applying ram-pressure stripping in massive halos ($\gtrsim 10^{14} M_\odot$) and halving the gas surface density threshold for star formation (Henriques et al. 2017); and the quenching of M_* galaxies is enhanced by increasing the AGN feedback efficiency at lower redshifts (Henriques et al. 2015). Both the GAEA and L-GALAXIES models have re-calibrated their model parameters to better reproduce observed stellar mass functions and quenched fractions at $0 < z < 3$, achieving success even in comparison with the latest observational constraints on quenched fractions from the DESI legacy imaging survey at $0.01 \leq z \leq 0.08$ (Fig. 13 of Meng et al. 2023). The physical recipes of *GABE* basically follow those of Guo et al. (2011), which are classic but somewhat outdated. We plan to update and re-calibrate our semi-analytic model in our future work, together with a detailed He abundance evolution of galaxies, which is necessary for the He-rich EHB formation model.

Nevertheless, EPS model is crucial or even more determinative in the reproduction of galaxy color distribution, which actually draws the allowed boundary of the color distribution (without considering dust attenuation). Semi-analytic model can only infer galaxy colors within the EPS model-allowed region according to each galaxy’s SFH. The galaxy color distributions adopting different EPS models could exhibit significant variation even with the same semi-analytic model, as shown in Figure 3. Therefore, in the near future, a well-constructed EPS model with various IMFs and metallicities, which has been observationally constrained by more recent observations (e.g. Sana et al. 2012; Moe & Di Stefano 2017), is necessary for the better reproduction of galaxy colors and would be a powerful tool to explore the possible binary origin of the UV-upturn phenomenon.

5 CONCLUSIONS

UV-upturn galaxies are elliptical galaxies (or central bulges in disk galaxies) with abnormally excessive flux in the FUV band, which is generally ascribed to the formation of EHB stars in old stellar populations. By using the semi-analytic model of galaxy formation and evolution *GABE* (Jiang et al. 2019), we embed the binary star formation model of EHB stars (Han et al. 2002, 2003, 2007; Zhang et al. 2020) within a framework of cosmological evolution to introduce variances of SFHs and explore the formation and evolution of UV-upturn galaxies in a cosmological context. We have gone through all physical mechanisms that are possibly related to the UV-upturn phenomenon, including stellar evolution (EPS models), initial mass function (IMF) and dust attenuation, as well as the age, metallicity and binary fractions of stellar populations in a galaxy,

attempting to figure out which processes play a more important role in forming/identifying a UV-upturn galaxy.

The photometric definition of UV-upturn galaxies of [Yi et al. \(2011\)](#) is adopted, and our conclusions can be summarized as follows.

- Having examined various EPS models including binary and single star versions of YUNNAN-II, BPASS, as well as GALAXEV, we find that only the YUNNAN-II model which has considered the formation of EHB stars through binary interactions (*YII-ehb*) could provide enough FUV flux in old stellar populations and reproduce a relatively large fraction of UV-upturn galaxies.

- EPS models with various IMFs result in almost identical UV-upturn phenomenon in the semi-analytic model. The variation of the high-mass end slope of IMF has almost no impact on quenched galaxies and only slightly influences the photometric properties of star-forming galaxies.

- After considering the dust attenuation, we find two categories of UV-upturn galaxies in the semi-analytic models: old metal-rich quenched elliptical galaxies which are intrinsic UV-upturn galaxies induced by EHB stars in their old stellar populations, and dusty star-forming galaxies which are relatively young galaxies and may also be photometrically identified as UV-upturn galaxies due to dust attenuation. The contribution of the dust attenuation channel depends on the detailed dust attenuation models adopted and ranges from 20% – 60%. Dust attenuation curves with strong UV bumps and steep slopes are helpful to the formation of dust induced UV-upturn galaxies.

- For the binary star model of [Han et al. \(2007\)](#), we find that the fraction of UV-upturn galaxies induced by EHB stars arising from binary interactions exhibits a strong dependence on both the age and metallicity of galaxies. Old and metal-rich galaxies have greater chances to be UV-upturned.

ACKNOWLEDGEMENTS

This work is supported by the National Key R&D Program of China (grant NO. 2022YFA1602902), the National Natural Science Foundation of China (grant Nos. 12433003, 11821303, 11973030), and China Manned Space Program through its Space Application System.

DATA AVAILABILITY

The Millennium Simulation data are available at Millennium Database⁸. The simulated galaxies catalogues produced from GABE, and data that support the figures are available from the corresponding author upon reasonable request.

REFERENCES

Akhil K. R., Kartha S. S., Kizhuprakkat N., Ujjwal K., P. N., 2024, *MNRAS*, **534**, 4063
 Ali S. S., Bremer M. N., Phillipps S., De Propriis R., 2018a, *MNRAS*, **476**, 1010
 Ali S. S., Bremer M. N., Phillipps S., De Propriis R., 2018b, *MNRAS*, **478**, 541

Ali S. S., Bremer M. N., Phillipps S., De Propriis R., 2018c, *MNRAS*, **480**, 2236
 Ali S. S., Bremer M. N., Phillipps S., De Propriis R., 2019, *MNRAS*, **487**, 3021
 Ali S. S., De Propriis R., Chung C., Phillipps S., Bremer M. N., 2021, *ApJ*, **923**, 12
 Ali S. S., et al., 2024, *ApJ*, **966**, 50
 Atlee D. W., Assef R. J., Kochanek C. S., 2009, *ApJ*, **694**, 1539
 Barber T., Meiksin A., Murphy T., 2007, *MNRAS*, **377**, 787
 Bertola F., Bressan A., Burstein D., Buson L. M., Chiosi C., di Serego Alighieri S., 1995, *ApJ*, **438**, 680
 Blagorodnova N., et al., 2017, *ApJ*, **834**, 107
 Blanton M. R., et al., 2005, *AJ*, **129**, 2562
 Bohlin R. C., Cornett R. H., Hill J. K., Hill R. S., Oconnell R. W., Stecher T. P., 1985, *ApJ*, **298**, L37
 Boissier S., Cucciati O., Boselli A., Mei S., Ferrarese L., 2018, *A&A*, **611**, A42
 Boselli A., et al., 2005, *ApJ*, **629**, L29
 Bressan A., Chiosi C., Fagotto F., 1994, *ApJS*, **94**, 63
 Brown T. M., Ferguson H. C., Davidsen A. F., 1995, *ApJ*, **454**, L15
 Brown T. M., Ferguson H. C., Deharveng J.-M., Jedrzejewski R. I., 1998, *ApJ*, **508**, L139
 Brown T. M., Bowers C. W., Kimble R. A., Ferguson H. C., 2000a, *ApJ*, **529**, L89
 Brown T. M., Bowers C. W., Kimble R. A., Sweigart A. V., Ferguson H. C., 2000b, *ApJ*, **532**, 308
 Brown T. M., Ferguson H. C., Smith E., Bowers C. W., Kimble R. A., Renzini A., Rich R. M., 2003, *ApJ*, **584**, L69
 Brown T. M., Smith E., Ferguson H. C., Sweigart A. V., Kimble R. A., Bowers C. W., 2008, *ApJ*, **682**, 319
 Bruzual G., Charlot S., 2003, *MNRAS*, **344**, 1000
 Bureau M., et al., 2011, *MNRAS*, **414**, 1887
 Burstein D., Bertola F., Buson L. M., Faber S. M., Lauer T. R., 1988, *ApJ*, **328**, 440
 Calzetti D., Armus L., Bohlin R. C., Kinney A. L., Koornneef J., Storchi-Bergmann T., 2000, *ApJ*, **533**, 682
 Carter D., Pass S., Kennedy J., Karick A. M., Smith R. J., 2011, *MNRAS*, **414**, 3410
 Chabrier G., 2003, *PASP*, **115**, 763
 Charlot S., Fall S. M., 2000, *ApJ*, **539**, 718
 Chen X., Han Z., 2004, *MNRAS*, **355**, 1182
 Chung C., Yoon S.-J., Lee Y.-W., 2011, *ApJ*, **740**, L45
 Chung C., Yoon S.-J., Lee Y.-W., 2017, *ApJ*, **842**, 91
 Clausen D., Wade R. A., Kopparapu R. K., O’Shaughnessy R., 2012, *ApJ*, **746**, 186
 Code A. D., 1969, *PASP*, **81**, 475
 Code A. D., Welch G. A., 1979, *ApJ*, **228**, 95
 Colless M., Dalton G., Maddox S., Sutherland W., et al. 2001, *MNRAS*, **328**, 1039
 Crossett J. P., Pimblett K. A., Stott J. P., Jones D. H., 2014, *MNRAS*, **437**, 2521
 Croton D. J., et al., 2006, *MNRAS*, **365**, 11
 D’Cruz N. L., Dorman B., Rood R. T., O’Connell R. W., 1996, *ApJ*, **466**, 359
 Davis M., Efstathiou G., Frenk C. S., White S. D. M., 1985, *ApJ*, **292**, 371
 Dawson K. S., et al., 2013, *AJ*, **145**, 10
 De Lucia G., Blaizot J., 2007, *MNRAS*, **375**, 2
 De Propriis R., Ali S. S., Chung C., Bremer M. N., Phillipps S., 2022, *MNRAS*, **512**, 1400
 Deharveng J. M., Laget M., Monnet G., Vuillemin A., 1976, *A&A*, **50**, 371
 Deharveng J. M., Boselli A., Donas J., 2002, *A&A*, **393**, 843
 Devriendt J. E. G., Guiderdoni B., Sadat R., 1999, *A&A*, **350**, 381
 Donahue M., et al., 2010, *ApJ*, **715**, 881
 Donas J., et al., 2007, *ApJS*, **173**, 597
 Dorman B., 1992, *ApJS*, **81**, 221
 Dorman B., O’Connell R. W., Rood R. T., 1995, *ApJ*, **442**, 105
 Eggleton P. P., 1971, *MNRAS*, **151**, 351
 Eldridge J. J., Stanway E. R., 2009, *MNRAS*, **400**, 1019
 Eldridge J. J., Izzard R. G., Tout C. A., 2008, *MNRAS*, **384**, 1109

⁸ <https://wwwmpa.mpa-garching.mpg.de/millennium/>

- Eldridge J. J., Stanway E. R., Xiao L., McClelland L. A. S., Taylor G., Ng M., Greis S. M. L., Bray J. C., 2017, *Publ. Astron. Soc. Australia*, **34**, e058
- Emsellem E., et al., 2004, *MNRAS*, **352**, 721
- Fitzpatrick E. L., Massa D., 1990, *ApJS*, **72**, 163
- Goldberg D., Mazeh T., 1994, *A&A*, **282**, 801
- Goudfrooij P., 2018, *ApJ*, **857**, 16
- Greggio L., Renzini A., 1990, *ApJ*, **364**, 35
- Greggio L., Renzini A., 1999, *Mem. Soc. Astron. Italiana*, **70**, 691
- Guo Q., et al., 2011, *MNRAS*, **413**, 101
- Han Z., 1998, *MNRAS*, **296**, 1019
- Han Z., Podsiadlowski P., Maxted P. F. L., Marsh T. R., Ivanova N., 2002, *MNRAS*, **336**, 449
- Han Z., Podsiadlowski P., Maxted P. F. L., Marsh T. R., 2003, *MNRAS*, **341**, 669
- Han Z., Podsiadlowski P., Lynas-Gray A. E., 2007, *MNRAS*, **380**, 1098
- Henriques B. M. B., White S. D. M., Thomas P. A., Angulo R. E., Guo Q., Lemson G., Springel V., 2013, *MNRAS*, **431**, 3373
- Henriques B. M. B., White S. D. M., Thomas P. A., Angulo R. E., Guo Q., Lemson G., Springel V., Overzier R., 2015, *MNRAS*, **451**, 2663
- Henriques B. M. B., White S. D. M., Thomas P. A., Angulo R. E., Guo Q., Lemson G., Wang W., 2017, *MNRAS*, **469**, 2626
- Henriques B. M. B., Yates R. M., Fu J., Guo Q., Kauffmann G., Srisawat C., Thomas P. A., White S. D. M., 2020, *MNRAS*, **491**, 5795
- Hernández-Pérez F., Bruzual G., 2013, *MNRAS*, **431**, 2612
- Hernández-Pérez F., Bruzual G., 2014, *MNRAS*, **444**, 2571
- Hirschmann M., De Lucia G., Fontanot F., 2016, *MNRAS*, **461**, 1760
- Horch E., Demarque P., Pinsonneault M., 1992, *ApJ*, **388**, L53
- Hurley J. R., Tout C. A., Pols O. R., 2002, *MNRAS*, **329**, 897
- Hurley J. R., Pols O. R., Aarseth S. J., Tout C. A., 2005, *MNRAS*, **363**, 293
- Iben Icko J., Rood R. T., 1970, *ApJ*, **161**, 587
- Iben Icko J., Tutukov A. V., 1986, *ApJ*, **311**, 753
- Jeong H., et al., 2012, *MNRAS*, **423**, 1921
- Jiang L., Helly J. C., Cole S., Frenk C. S., 2014, *MNRAS*, **440**, 2115
- Jiang Z., Wang J., Gao L., Zhang F.-H., Guo Q., Wang L., Pan J., 2019, *Research in Astronomy and Astrophysics*, **19**, 151
- Kauffmann G., Colberg J. M., Diaferio A., White S. D. M., 1999, *MNRAS*, **303**, 188
- Kaviraj S., et al., 2007, *ApJS*, **173**, 619
- King I. R., et al., 1992, *ApJ*, **397**, L35
- Kriek M., Conroy C., 2013, *ApJ*, **775**, L16
- Le Cras C., Maraston C., Thomas D., York D. G., 2016, *MNRAS*, **461**, 766
- Lee Y.-W., 1994, *ApJ*, **430**, L113
- Loncoe I., Maraston C., Thomas D., Longhetti M., Parikh T., Guarnieri P., Comparat J., 2020, *MNRAS*, **492**, 326
- Loubser S. I., Sánchez-Blázquez P., 2011, *MNRAS*, **410**, 2679
- Ma X., Hopkins P. F., Kasen D., Quataert E., Faucher-Giguère C.-A., Kereš D., Murray N., Strom A., 2016, *MNRAS*, **459**, 3614
- Mahajan S., et al., 2020, *MNRAS*, **491**, 398
- Maraston C., 2005, *MNRAS*, **362**, 799
- Martin D. C., et al., 2005, *ApJ*, **619**, L1
- Mathis J. S., Mezger P. G., Panagia N., 1983, *A&A*, **128**, 212
- Mazeh T., Goldberg D., Duquennoy A., Mayor M., 1992, *ApJ*, **401**, 265
- McDonald I., Zijlstra A. A., 2015, *MNRAS*, **448**, 502
- Meng J., Li C., Mo H. J., Chen Y., Jiang Z., Xie L., 2023, *ApJ*, **944**, 75
- Miglio A., et al., 2012, *MNRAS*, **419**, 2077
- Miller G. E., Scalo J. M., 1979, *ApJS*, **41**, 513
- Moe M., Di Stefano R., 2017, *ApJS*, **230**, 15
- Morrissey P., et al., 2005, *ApJ*, **619**, L7
- Noll S., et al., 2009a, *A&A*, **499**, 69
- Noll S., Burgarella D., Giovannoli E., Buat V., Marcellac D., Muñoz-Mateos J. C., 2009b, *A&A*, **507**, 1793
- O’Connell R. W., 1999, *ARA&A*, **37**, 603
- O’Connell R. W., et al., 1992, *ApJ*, **395**, L45
- Ohl R. G., et al., 1998, *ApJ*, **505**, L11
- Park J.-H., Lee Y.-W., 1997, *ApJ*, **476**, 28
- Peacock M. B., Zepf S. E., Maccarone T. J., Kundu A., Knigge C., Dieball A., Strader J., 2018, *MNRAS*, **481**, 3313
- Petty S. M., et al., 2013, *AJ*, **146**, 77
- Phillipps S., et al., 2020, *MNRAS*, **492**, 2128
- Pols O. R., Marinus M., 1994, *A&A*, **288**
- Ree C. H., et al., 2007, *ApJS*, **173**, 607
- Rettura A., et al., 2006, *A&A*, **458**, 717
- Rettura A., et al., 2011, *ApJ*, **732**, 94
- Rich R. M., et al., 2005, *ApJ*, **619**, L107
- Rosenfield P., et al., 2012, *ApJ*, **755**, 131
- Salim S., Narayanan D., 2020, *ARA&A*, **58**, 529
- Salim S., Rich R. M., 2010, *ApJ*, **714**, L290
- Salim S., et al., 2007, *ApJS*, **173**, 267
- Salpeter E. E., 1955, *ApJ*, **121**, 161
- Salvador-Rusiñol N., Vazdekis A., La Barbera F., Beasley M. A., Ferreras L., Negri A., Dalla Vecchia C., 2020, *Nature Astronomy*, **4**, 252
- Sana H., et al., 2012, *Science*, **337**, 444
- Sandage A. R., 1953, *AJ*, **58**, 61
- Savage B. D., Mathis J. S., 1979, *ARA&A*, **17**, 73
- Seaton M. J., 1979, *MNRAS*, **187**, 73
- Smith R. J., Lucey J. R., Carter D., 2012, *MNRAS*, **421**, 2982
- Sodré L., Ribeiro da Silva A., Santos W. A., 2013, *MNRAS*, **434**, 2503
- Spergel D. N., et al., 2003, *ApJS*, **148**, 175
- Springel V., White S. D. M., Tormen G., Kauffmann G., 2001, *MNRAS*, **328**, 726
- Springel V., et al., 2005, *Nature*, **435**, 629
- Stanway E. R., Eldridge J. J., 2018, *MNRAS*, **479**, 75
- Vazdekis A., Casuso E., Peletier R. F., Beckman J. E., 1996, *ApJS*, **106**, 307
- Vazdekis A., Koleva M., Ricciardelli E., Röck B., Falcón-Barroso J., 2016, *MNRAS*, **463**, 3409
- Wang L., et al., 2017, *MNRAS*, **468**, 4579
- Webbink R. F., 1984, *ApJ*, **277**, 355
- Welch G. A., 1982, *ApJ*, **259**, 77
- Werle A., et al., 2020, *MNRAS*, **497**, 3251
- White S. D. M., Frenk C. S., 1991, *ApJ*, **379**, 52
- Williams K. A., Canton P. A., Bellini A., Bolte M., Rubin K. H. R., Gianninas A., Kilic M., 2018, *ApJ*, **867**, 62
- Xie L., De Lucia G., Hirschmann M., Fontanot F., 2020, *MNRAS*, **498**, 4327
- Yi S., Demarque P., Oemler Augustus J., 1997, *ApJ*, **486**, 201
- Yi S., Demarque P., Oemler Augustus J., 1998, *ApJ*, **492**, 480
- Yi S. K., Lee J., Sheen Y.-K., Jeong H., Suh H., Oh K., 2011, *ApJS*, **195**, 22
- York D. G., et al., 2000, *AJ*, **120**, 1579
- Zhang F., Han Z., Li L., Hurley J. R., 2004, *A&A*, **415**, 117
- Zhang F., Han Z., Li L., Hurley J. R., 2005, *MNRAS*, **357**, 1088
- Zhang F., Han Z., Li L., Guo J., Zhang Y., 2010, *Ap&SS*, **329**, 249
- Zhang F., Han Z., Li L., 2020, in Boquien M., Lusso E., Gruppioni C., Tissera P., eds, Vol. 341, *Panchromatic Modelling with Next Generation Facilities*. pp 35–38, doi:10.1017/S174392131900262X
- Zhou S., et al., 2019, *MNRAS*, **485**, 5256

This paper has been typeset from a $\text{\TeX}/\text{\LaTeX}$ file prepared by the author.